Microwave spectroscopy of the Yb $6s(n+3)d \rightarrow 6sng$, $6snh$, and $6sni$ transitions

F. Niyaz,[1] J. Nunkaew,[2,3,*] and T. F. Gallagher[1]

[1]*Department of Physics, University of Virginia, Charlottesville, Virginia 22904, USA*
[2]*Department of Physics and Materials Science, Faculty of Science, Chiang Mai University, Chiang Mai 50200, Thailand*
[3]*Center of Excellence in Materials Science and Technology, Chiang Mai University, Chiang Mai 50200, Thailand*

Using a microwave and radio frequency resonance approach we observe the transitions of ytterbium from the $6s(n+3)d$ states to the $6sn\ell$ states for $4 \leqslant \ell \leqslant 6$ and $28 \leqslant n \leqslant 33$. The energies of the $6sn\ell$ states of $\ell \geqslant 4$ are determined from the observed intervals and the known values of the $6snd$ energies. We use a nonadiabatic core polarization model to analyze the energy levels to determine the dipole (α_d) and quadrupole (α_q) polarizabilities of the ground state of Yb^+. We find the values $\alpha_d = 60.51(10)a_0^3$ and $\alpha_q = 672(28)a_0^5$.

I. INTRODUCTION

The Yb^+ ion is of great interest for use in an optical frequency standard, the study of parity nonconservation (PNC), and the study of the violation of Lorentz symmetry [1–15]. For these applications it is critical to know the electric multipole moments connecting the Yb^+ ground state to its first few excited states. In a $^{171}Yb^+$ optical frequency standard [1–12] the leading contribution to the systematic uncertainty of the frequency is the blackbody radiation (BBR) shift [13]. At an operating temperature of 300 K, the BBR shift is measured to be $-0.36(7)$ Hz [5]. The $^2S_{1/2}(F=0)$-$^2D_{3/2}(F'=2)$ transition frequency is realized with an uncertainty of 1.1×10^{-16} that is mainly from the BBR shift uncertainty [13]. The BBR shift is proportional to the difference in the dipole polarizabilities of the ionic $^2S_{1/2}$ and $^2D_{3/2}$ states. The largest contribution to the uncertainty of the BBR shift is the uncertainty of the polarizabilities of the ionic states [13]. Therefore, it is essential to determine accurate values of the polarizabilities of the ionic states. In the study of PNC, the Yb^+ ion is one of the candidates for testing the standard model. The dipole (E1) matrix elements of Yb^+ $6s_{1/2}$-$6p_{1/2}$ and $6s_{1/2}$-$6p_{3/2}$ and the quadrupole (E2) matrix elements of Yb^+ $6s_{1/2}$-$5d_{3/2}$ and $6s_{1/2}$-$5d_{5/2}$ are important in the calculation of PNC in the Yb^+ ion [15]. Since these matrix elements are the most important contributions to the dipole and quadrupole polarizabilities α_d and α_q of the ground state of Yb^+, measurements of these polarizabilities constrain the possible values of these matrix elements.

We have determined the ground-state Yb^+ polarizabilities by measuring energies of the high-ℓ, $\ell \geqslant 5$, $6sn\ell$ states of Yb. When the Rydberg electron is in a high-ℓ, $\ell \geqslant 5$, state, there is no core penetration [16,17], but the $n\ell$ Rydberg electron produces a quasistatic electric field at the ion core, which polarizes the Yb^+ ion core and depresses the $6sn\ell$ Rydberg state energy from the hydrogenic $n\ell$ level [18]. Hence, the polarizabilities of the ion core can be measured by measuring the depression of the energies of the Yb Rydberg $6sn\ell$ states below the $n\ell$ hydrogenic level.

Here we report the $6s(n+3)d\,^1D_2 \rightarrow 6sn\ell$, $4 \leqslant \ell \leqslant 6$, intervals observed by microwave spectroscopy. Using the known $6s(n+3)d$ energy levels [19], we determine the energy levels of the $6sn\ell$ states and their quantum defects. We use a nonadiabatic core polarization model to analyze the $6sn\ell$ energy levels of $\ell = 5$ and 6 to determine the Yb^+ $6s$ dipole and quadrupole polarizabilities. In the sections that follow we describe the experimental approach, our observations, and the data analysis. Finally, we compare our polarizabilities to those obtained previously.

II. EXPERIMENTAL APPROACH

In this experiment atoms in a thermal beam of neutral Yb are excited to Rydberg states using two pulsed dye lasers at a 20 Hz repetition rate. We use natural Yb, and for the analysis we assume that we have the most common isotope, ^{174}Yb. The first laser, fixed at 398.91 nm, drives the ground-state $6s^2\,^1S_0$ atoms to the $6s6p\,^1P_1$ state, and a tunable laser at about 396 nm drives the atoms to $6s(n+3)d\,^1D_2$ states. The atoms in the $6s(n+3)d\,^1D_2$ states are further excited by microwave and radio frequency (RF) photons to the higher angular momentum $6sn\ell$ states. The relevant energy levels of Yb are shown in Fig. 1(a). The Yb beam and the two copropagating laser beams cross at a right angle between two horizontal plates 1.5 cm apart, defining the region in which the Yb Rydberg atoms interact with the microwave and RF pulses. As shown by Fig. 1(b), a 1 μs long microwave pulse starts 50 ns after the second laser pulse to excite the atoms to the nearby $6sng$ state by a two-photon transition. For the three-photon transitions $6s(n+3)d \rightarrow 6snh$, a 1 μs long RF pulse is added at the same time as the microwave pulse. The $6s(n+3)d \rightarrow 6sni$ transition is driven by adding a bias field of 100–200 mV/cm in addition to the microwave and RF pulses.

The microwave power is generated by an Agilent 83620A synthesized sweep generator that produces a continuous wave (CW) output from 10 MHz to 20 GHz. A General Microwave DM862D switch is then used to produce the

———
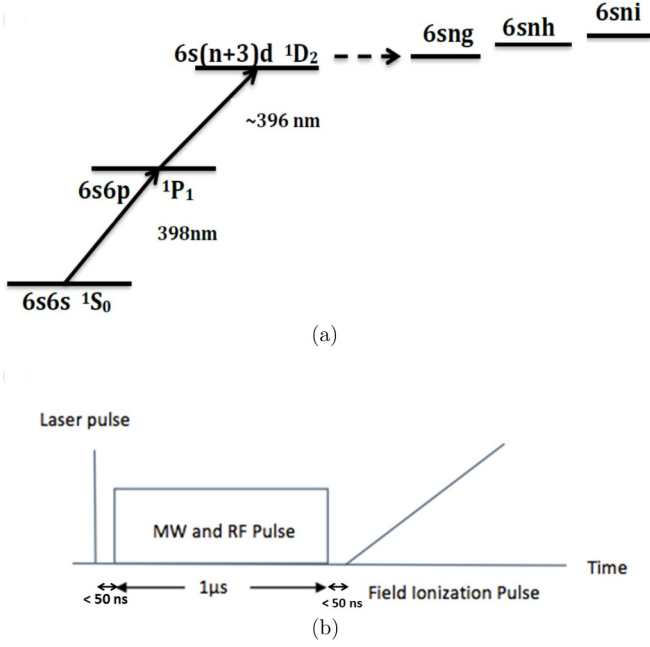*Corresponding author: jn8h@virginia.edu

FIG. 1. (a) Energy levels and (b) timing of the experiment.

microwave pulses. Several frequency multipliers—a Narda DBS2640X220 active doubler, a Narda DBS4060X410 active quadrupler, a Pacific Millimeter V2WO passive doubler, a Pacific Millimeter W3WO passive tripler, and a custom-made Pacific Millimeter D3WO passive tripler—are used to multiply the synthesizer frequency to the desired frequency. The microwave pulse propagates from the frequency multiplier through a WR28 waveguide feedthrough to a WR28 horn inside the vacuum chamber. The RF frequency source is a swept signal generator of the Agilent Technologies 8360B series that is used to generate a pulsed output of $\sim$20 mW over a range of 3–8 GHz and is delivered to a WR 187 horn inside the vacuum chamber by coaxial cable.

We nulled the stray electric field in the vertical direction by applying a bias voltage to the lower plate defining the interaction region. A typical applied voltage is 100 mV, corresponding to a 67 mV/cm field. We have measured the horizontal stray field by replacing the upper plate with a split plate, allowing the application of a horizontal field. Using this approach we determined the horizontal stray fields to be <10 mV/cm. For all the measurements the vertical field was nulled, and the horizontal field leads to a shift of at most 170 kHz in the worst case, the $6s36d$-$6s33i$ transition. In all cases the shifts are less than the measurement uncertainties.

As shown in Fig. 1(b), 50 ns after the microwave pulse, a large negative voltage pulse is applied to the bottom plate to field-ionize the Rydberg atoms. The amplitude of the field pulse is chosen to allow the temporal separation of the ionization signals from the initial and final states of the transitions. The final states of the transitions are lower in energy than the initial $6s(n+3)d$ states and ionize at higher fields. Since the high-ℓ $6sn\ell$ states lie energetically between the initial and final states of the microwave transitions, it is straightforward to separate the two field ionization signals [20]. The freed electrons pass through a hole in the top aluminum plate

and are detected by a microchannel plate (MCP) detector. The MCP signal is recorded by a gated integrator as one of the synthesizers is swept over the resonance frequency over many shots of the lasers. The frequency sweeps are repeated until an acceptable signal-to-noise ratio is obtained.

III. EXPERIMENTAL OBSERVATIONS

A. Two-photon $6s(n+3)d \to 6sng$ intervals

We observed the two-microwave-photon $6s(n+3)d \to 6sng$ transitions for $28 \leqslant n \leqslant 33$. Figure 2 shows a typical resonance, the $6s34d \to 6s31g$ transition at the relative microwave power of 0.008. At relative power 1 the power output of the source is 15 dBm (31 mW). Its linewidth is 1 MHz, which is the transform limited linewidth. There was no attempt to eliminate the earth's magnetic field. However, the states $6s(n+3)d\,{}^1D_2$ and $6sng\,{}^1G_4$ are singlet states, and they have the same Landé g_j factors. Therefore, all the $\Delta m_j = 0$ transitions occur at the same frequency, yielding narrow lines [21]. Since there is an AC Stark shift, we observed the microwave resonances at different microwave powers and extrapolated to zero power as shown in Fig. 3. The largest AC shift we observed was $\sim$0.5 MHz. The observed intervals, twice the two-photon frequencies extrapolated to zero power, are given in Table I.

B. Three-photon $6s(n+3)d \to 6snh$ intervals

The three-photon transitions were driven by two microwave photons and one RF photon. To observe the three-photon resonances, the microwave frequency was swept near the two-photon $(n+3)d$-ng transitions and the RF frequency was fixed approximately 100–500 MHz from the expected $6sng$-$6snh$ interval. The RF frequency was in the range of 3–6 GHz for the n states of interest. To verify that the transitions observed were three-photon $6s(n+3)d \to 6snh$ transitions, we varied the RF frequency over a range of ±5 MHz. At each
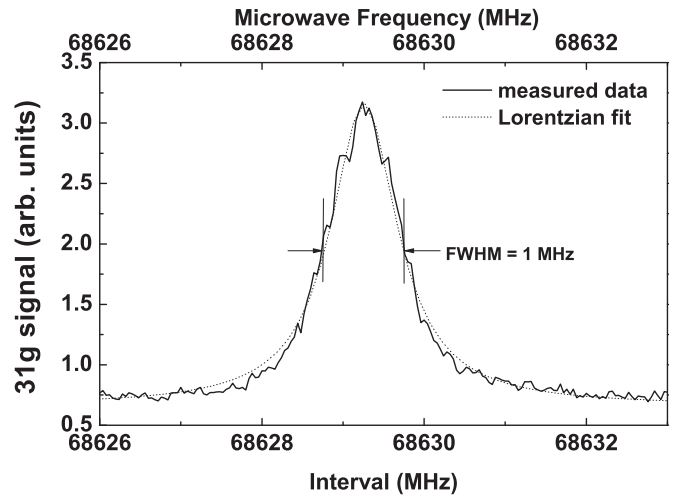

FIG. 2. Two-photon $6s34d \to 6s31g$ resonance at the relative microwave power of 0.008. The linewidth of the resonance is 1 MHz, which is the transform limited linewidth of a 1 μs microwave pulse. At the peak of the resonance we estimate that $\sim$100 atoms undergo the microwave transition on each laser shot.
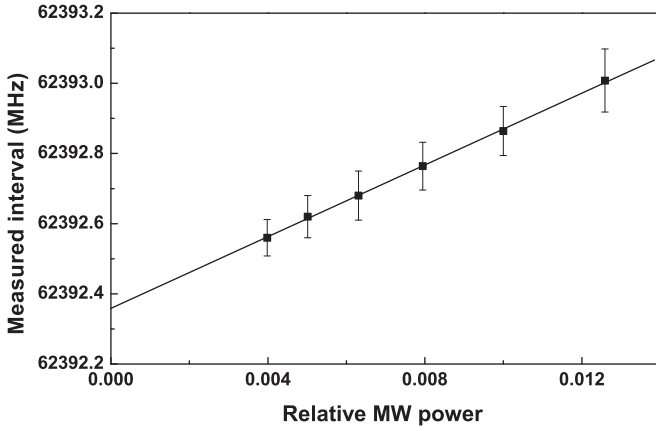
FIG. 3. Extrapolation of the two-photon $6s35d \rightarrow 6s32g$ resonance to zero microwave power.
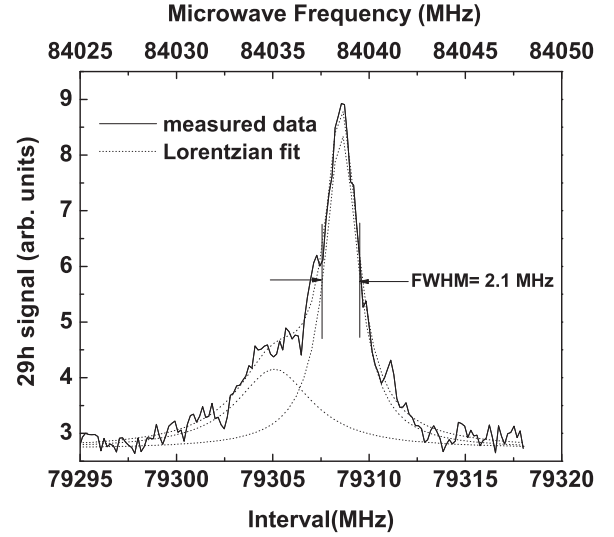

FIG. 4. Three-photon $6s32d \rightarrow 6s29h$ resonances at relative microwave power and relative RF power of 0.562 and 0.126, respectively. The RF frequency is 4730 MHz and the microwave frequency is scanned as shown by the scale at the top of the figure. The linewidth of the resonance is 2.1 MHz. The subsidiary feature at 79 305 MHz is due to a $\Delta m \neq 0$ transition driven by perpendicular RF and microwave fields.

RF frequency, the microwave frequency was scanned, and we verified that the difference of twice the microwave frequency and the RF frequency was constant over the RF range used. A typical resonance, the $6s32d$-$6s29h$ transition, is shown in Fig. 4. The resonance is not as narrow as that shown in Fig. 2, possibly because the $6snh$ state is not a singlet state, with the result that the resonance is broadened by the earth's field.

We expected to observe doublets of approximately equal intensity, due to the K splitting, as observed in Ca, Sr, and Ba [16,17,22]. Using the adiabatic expansion method we estimated the K splittings for the Yb $6s30h$ and $6s30g$ states to be 60 and 10 MHz, respectively [23]. In spite of a thorough search we only observed one strong feature, as shown in Fig. 4. The small feature at 79 305 MHz in Fig. 4 is due to $\Delta m \neq 0$ transitions, which occur due to the presence of both parallel and perpendicular microwave and RF fields. Since both features extrapolate to the same zero-power interval, we ignore the weaker feature.

There are AC Stark shifts due to both the microwave and RF fields, leading to maximum shifts of about 20 MHz. We verified that the AC Stark shifts due to the RF and microwave fields were additive, and we then employed the following approach. We observed the resonances at different RF powers while the microwave power was kept constant. The zero RF power resonance frequency at that microwave power was determined by extrapolating the observed resonances linearly as shown in Fig. 5(a). We then varied the microwave power to find the zero RF power resonances at different microwave powers. The zero RF power data were extrapolated to zero microwave power to obtain the resonance frequency at zero

RF and microwave powers, as shown in Fig. 5(b). In Table II we present the approximate RF and microwave frequencies used and the $6s(n+3)d$-$6snh$ intervals extrapolated to zero RF and microwave powers.

C. Three-photon and static-field $6s(n+3)d \rightarrow 6sni$ intervals

We could not produce enough microwave and RF power to drive the four-photon $6s(n+3)d \rightarrow 6sni$ transitions. Hence, these transitions were driven by three photons in the presence of a static field in the z direction. For these transitions the microwave frequency was kept constant near the two-photon $6s(n+3)d \rightarrow 6sng$ resonances, and the RF frequency was swept to observe the $6s(n+3)d \rightarrow 6sni$ transitions. As for the $6snh$ states, we do not observe a K splitting, rather a single resonance, typified by the $6s32d$-$6s29i$ resonance shown in Fig. 6, which was taken at a static field of 121.8 mV/cm, with relative microwave and RF powers of 0.9 and 0.1, respectively. The linewidth of the resonance is 5.3 MHz. The minimum linewidth of the $6s(n+3)d$-$6sni$ transitions was 3 MHz, presumably due to the earth's field. Since the Rabi frequency for the transition is proportional to the static

TABLE I. $6s(n+3)d$-$6sng$ observed intervals.

n	Interval (MHz)
28	93 198.90(5)
29	83 854.12(8)
30	75 730.23(12)
31	68 628.92(6)
32	62 392.36(7)
33	56 891.84(7)

TABLE II. $6s(n+3)d$-$6snh$ observed intervals.

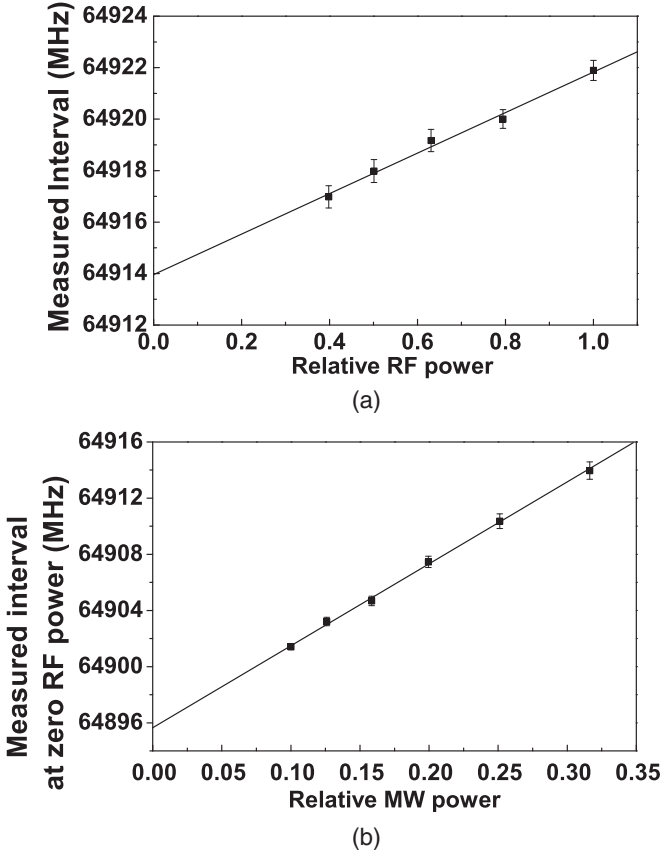| n	Approx. RF frequency (MHz)	Approx. MW frequency (MHz)	$6s(n+3)d \rightarrow$ $6snh$ interval (MHz)
29	4730	42 010	79 298.88(24)
30	4490	38 050	71 613.62(30)
31	4200	34 550	64 895.66(37)
32	4190	31 600	58 999.46(38)
33	4200	29 000	53 788.98(38)

FIG. 5. Extrapolation of the three-photon $6s34d \rightarrow 6s31h$ resonance to zero microwave power and zero RF power. (a) The relative microwave power was kept at 0.316; the resonances were observed at different RF powers. The observed data were extrapolated to find the resonance at zero RF power. (b) The same process as (a) was repeated at several microwave powers. The zero RF power data at different microwave powers were extrapolated to obtain the resonance at zero RF and microwave powers.

field, the resonances broaden with increasing static field. The static field was varied over the range of 0–150 mV/cm, which causes a frequency shift as large as 40 MHz. To eliminate the AC Stark shift of a $6s(n + 3)d$ to $6sni$ transition at a given value of static field we followed the same procedure we used for the three-photon $6s(n + 3)d \rightarrow 6snh$ transitions, resulting in the $6s(n + 3)d \rightarrow 6sni$ intervals at zero microwave and RF powers for that static field. The RF and microwave power extrapolations are shown in Figs. 7(a) and 7(b). Both microwave and RF powers lead to frequency shifts of up to ~5 MHz. The zero-power intervals were then extrapolated to zero static field, as shown by Fig. 8, a linear plot of the $6s(n + 3)d \rightarrow 6sni$ interval versus the square of the static field. In Table III we give the typical RF and microwave frequencies and the $6s(n + 3)d$-$6sni$ intervals extrapolated to zero static field.

IV. ENERGIES AND QUANTUM DEFECTS

Using the $6snd$ $^1D_2$ quantum defects extracted from the multichannel quantum defect theory analysis of Ref. [19] and the ionization limit of 50 443.07041(25) cm^{-1} [19] yields the $6s(n + 3)d$ binding energies of Table IV.
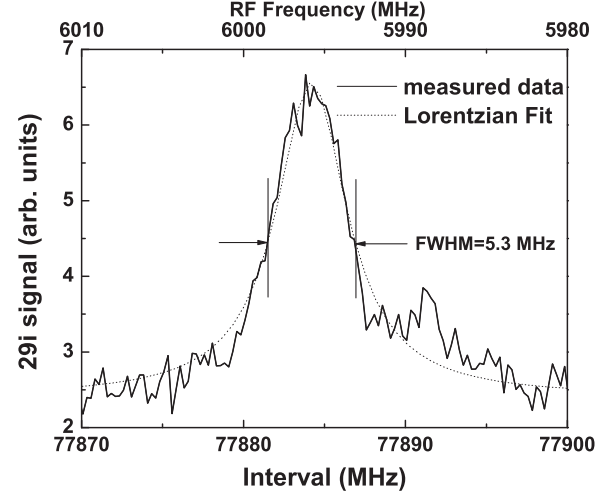

FIG. 6. Four-photon $6s32d \rightarrow 6s29i$ resonance at static field of 121.8 mV/cm, relative microwave power 0.891, and relative RF power 0.1. The microwave frequency is 41 940 MHz, and the RF frequency is scanned as shown by the upper scale. With the same microwave and RF powers the linewidth is 3 MHz at low static field, but at this static field the resonance is power broadened to 5.3 MHz since the Rabi frequency is proportional to the static field.

Combining these energies with the intervals given in the previous section we find the $6sn\ell$ binding energies given in Table V, where we also give the hydrogenic binding energies of $28 \leqslant n \leqslant 33$, calculated using the Rydberg constant for ^{174}Yb, $R_{Yb} = 3\,289\,831\,526.526$ MHz.

The binding energies of Table V can be used to determine the quantum defects of the $6sn\ell$ states. The energy of a $6sn\ell$ state is given by

$$W_{6sn\ell} = \frac{-R_{Yb}}{(n - \delta_\ell)^2}. \tag{1}$$

The quantum defect δ_ℓ of an unperturbed Rydberg series can be expressed using a Ritz expansion.

Explicitly,

$$\delta_\ell = \delta_{\ell 0} + \frac{\delta_{\ell 1}}{(n - \delta_{\ell 0})^2}. \tag{2}$$

Fitting the $6sng$, $6snh$, and $6sni$ energies of Table V to Eqs. (1) and (2) leads to the quantum defects of the $6sn\ell$ states and the quantum defect parameters shown in Tables VI and VII, respectively.

TABLE III. $6s(n + 3)d$-$6sni$ observed intervals.

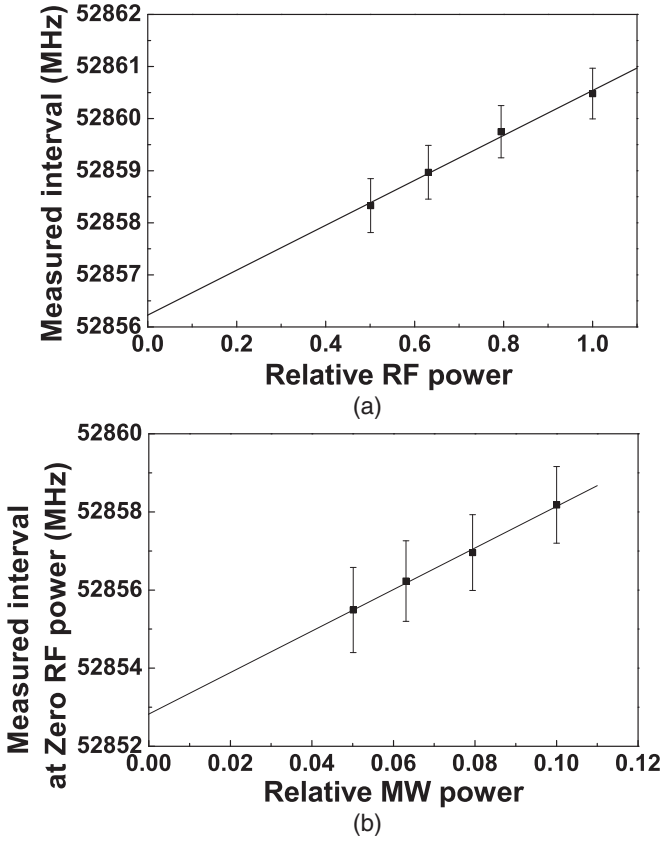| n	Approx. RF frequency (MHz)	Approx. MW frequency (MHz)	$6s(n + 3)d \rightarrow 6sni$ interval (MHz)
29	6010	41 940	77 866.0(28)
30	5440	37 880	70 318.78(36)
31	4930	34 330	63 726.60(85)
32	4490	31 210	57 934.35(55)
33	4080	28 460	52 836.4(25)

FIG. 7. Extrapolation of the three-photon $6s36d \to 6s33i$ resonance in the static field of 83.33 mV/cm to zero microwave power and zero RF power. (a) The relative microwave power was kept at 0.0631; the resonances were observed at different RF powers. The observed data were extrapolated to find the resonance at zero RF power. (b) The same process as (a) was repeated at a few different microwave powers. The zero RF power data at different microwave powers were extrapolated to obtain the $6s36d \to 6s33i$ interval at zero RF and microwave powers.

V. CORE POLARIZATION ANALYSIS

The energy depression below the hydrogenic energy and quantum defects of nonhydrogenic Rydberg states arise from penetration and polarization of the ion core by the Rydberg electron. Penetration only occurs for Rydberg states of low ℓ; for high-ℓ states the quantum defects are only due to the polarization of the ion core by the electric field and field gradient from the Rydberg electron. The polarization energy

TABLE IV. Quantum defects and binding energy of $6s(n + 3)d$ states.

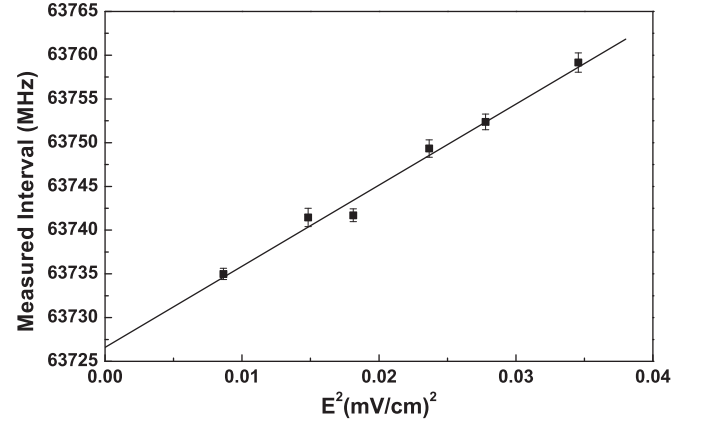| $(n + 3)$	Quantum defects	Binding energy (MHz)
31	2.710792	4 110 837.1(2.4)
32	2.710816	3 834 998.7(2.4)
33	2.710879	3 586 003.7(2.4)
34	2.710960	3 360 484.1(2.4)
35	2.711049	3 155 582.3(2.4)
36	2.711141	2 968 861.1(2.4)

FIG. 8. Frequency of the $6s34d \to 6s31i$ interval vs squared bias field applied in the z direction. The zero-field frequency is 63 726.60(85) MHz.

is given by

$$W_{\mathrm{pol},n\ell} = W_{6sn\ell} - W_{nH}, \tag{3}$$

where $W_{\mathrm{pol},n\ell}$ is the polarization energy, $W_{6sn\ell}$ is the energy level of the $n\ell$ Rydberg state, and W_{nH} is the hydrogenic energy level of the n state. If the Rydberg electron moves slowly relative to the electrons in the ion core (the adiabatic approximation) the polarization energy can be written in atomic units as [18]

$$W_{\mathrm{pol},n\ell} = -\tfrac{1}{2}\alpha_d \langle r^{-4}\rangle_{n\ell} - \tfrac{1}{2}\alpha_q \langle r^{-6}\rangle_{n\ell}, \tag{4}$$

where α_d and α_q are the dipole and quadrupole polarizabilities of the Yb$^+$ $6s$ core, respectively. The expectation values of r^{-4} and r^{-6} are the squares of the field and the field gradient at the core from the Rydberg electron in the $n\ell$ state. Assuming the Rydberg $n\ell$ electron to be hydrogenic, we can use known analytic expressions for the expectation values $\langle r^{-4}\rangle_{n\ell}$ and $\langle r^{-6}\rangle_{n\ell}$. Therefore, by measuring $W_{pol,n\ell}$ for several nonpenetrating high-ℓ states we can determine the polarizabilities α_d and α_q of the ion core.

We can rewrite Eq. (4) in the experimentally convenient form as [24]

$$W_{\mathrm{pol},n\ell} = -\alpha_d P_{n\ell} - \alpha_q P Q_{n\ell}, \tag{5}$$

where

$$P_{n\ell} = R_{\mathrm{Yb}} \langle r^{-4}\rangle_{n\ell} \tag{6}$$

and

$$Q_{n\ell} = \frac{\langle r^{-6}\rangle_{n\ell}}{\langle r^{-4}\rangle_{n\ell}}. \tag{7}$$

We can express Eq. (5) as

$$-\frac{W_{\mathrm{pol},n\ell}}{P_{n\ell}} = \alpha_d + \alpha_q Q_{n\ell}. \tag{8}$$

From Eq. (8), we can extract the values of α_d and α_q from a graph of $-W_{\mathrm{pol},n\ell}/P_{n\ell}$ vs $Q_{n\ell}$; α_d and α_q are the intercept and slope of a line through the data points.

As pointed out by Van Vleck and Whitelaw, the adiabatic core polarization model is a limiting case of a more general model. The polarization energy shift of the $n\ell$ state from the

TABLE V. Binding energies of $6sn\ell$ states and the hydrogenic energy.

n	$6sng$ (MHz)	$6snh$ (MHz)	$6sni$ (MHz)	Hydrogenic (MHz)
28	4 204 036.0(2.4)			4 196 213.7
29	3 918 852.8(2.4)	3 914 297.6(2.4)	3 912 864.7(3.7)	3 911 809.2
30	3 661 733.9(2.4)	3 657 617.3(2.4)	3 656 322.4(2.4)	3 655 368.4
31	3 429 113.0(2.4)	3 425 379.7(2.4)	3 424 210.7(2.6)	3 423 341.9
32	3 217 974.6(2.4)	3 214 581.7(2.4)	3 213 516.6(2.5)	3 212 726.1
33	3 025 752.9(2.4)	3 022 650.1(2.4)	3 021 697.5(3.5)	3 020 965.6

hydrogenic level is the second-order shift due to the multipole expansion of the Coulomb interaction between the ion core and the $n\ell$ Rydberg electron [25]. The adiabatic equation, Eq. (4), is the limiting case of the second-order shift when the energies of the excited ion core are much greater than the spread in energies of the relevant Rydberg states. To make this notion more concrete we use the dipole polarization energy of the $6s30h$ state of Yb as an example. Consider the simple picture of the Yb energy levels shown in Fig. 9. For each energy level of the Yb$^+$ core (NL, bold line), there are Rydberg series ($NLn\ell$) converging to the ionic level from below and the continua ($NL\epsilon\ell$) above the ionic level. The dipole polarization energy of the $6s30h$ state comes from the dipole coupling of the $6s30h$ state to the $Npng$, $Np\epsilon g$, $Npni$, and $Np\epsilon i$ states. The total dipole shift due to the levels associated with the ionic Np state is calculated by using the dipole coupling in second-order perturbation theory and summing over all n and integrating over the continua ϵ. The summation and integration span the energy range Δ in Fig. 9. In the limit where the span of energy is much less than the ionic energy level separation, $\Delta \ll \Omega$, the adiabatic equation, Eq. (4), is recovered.

The adiabatic core polarization model works well for the alkali metals where the energies of the excited ionic states are much greater than the spread in energy of the relevant Rydberg states. However, the adiabatic core polarization model breaks down when applied to the alkaline-earth metals and Yb, where the energies of the ionic excited states are comparable to the spread in energy of the relevant Rydberg states. For example, the energies of the low-lying excited states of Li$^+$ and Na$^+$ exceed 30 eV while the energy span of the relevant Rydberg states is less than 1 eV. In contrast, the low-lying ionic states of Yb$^+$ have energies less than 4 eV, while the relevant Rydberg states still span an energy range approaching 1 eV. Therefore, we must take the nonadiabatic effect into account. It can be done in several ways. One is the adiabatic expansion method, in which expectation values of higher inverse powers of r

are used [26]. An alternative, which we have used here, is to introduce the nonadiabatic factors k_d and k_q so that Eq. (4) becomes [27]

$$W_{\mathrm{pol},n\ell} = -\tfrac{1}{2}\alpha_d k_d \langle r^{-4}\rangle_{n\ell} - \tfrac{1}{2}\alpha_q k_q \langle r^{-6}\rangle_{n\ell}. \quad (9)$$

The numerical factors k_d and k_q are the ratios of the perturbation theory sums to the expectation values $\langle r^{-4}\rangle_{n\ell}$ and $\langle r^{-6}\rangle_{n\ell}$. Yb is similar to alkaline earth atoms in that the largest radial matrix elements connecting the Yb$^+$ ground state to the Np and Nd states are the $\langle 6s|r|6p\rangle$ and $\langle 6s|r^2|5d\rangle$ matrix elements. Accordingly, the largest contributions to α_d and α_q come from the dipole and quadrupole couplings to the $6pn'\ell$ and $5dn'\ell$ states. To a good approximation α_d and α_q are only due to these couplings, so we assume this to be the case, although it introduces the need for small corrections to the values we obtain for α_d and α_q. With the assumption that only the $6pn'\ell$ and $5dn'\ell$ states contribute to the k_d and k_q sums, they are given by [27]

$$k_d = \frac{(W_{6p} - W_{6s})}{\langle n\ell|\frac{1}{r_2^4}|n\ell\rangle} \left[\frac{\ell}{2\ell+1} \sum_{n'} \frac{\left|\langle n\ell|\frac{1}{r_2^2}|n'\ell-1\rangle\right|^2}{W_{6pn'\ell-1} - W_{6sn\ell}} + \frac{\ell+1}{2\ell+1} \right.$$
$$\left. \times \sum_{n'} \frac{\left|\langle n\ell|\frac{1}{r_2^2}|n'\ell+1\rangle\right|^2}{W_{6pn'\ell+1} - W_{6sn\ell}} \right] \quad (10)$$

and

$$k_q = \frac{5(W_{5d} - W_{6s})}{\langle n\ell|\frac{1}{r_2^6}|n\ell\rangle} \left\{ \frac{3}{10(4\ell^2-\ell)(2\ell+3)} \right.$$
$$\times \left[(2\ell-1)(\ell+1)(\ell+2) \sum_{n'} \frac{\left|\langle n\ell|\frac{1}{r_2^3}|n'\ell+2\rangle\right|^2}{W_{5dn'\ell+2} - W_{6sn\ell}} \right.$$
$$+ \frac{2(\ell^2+\ell)(2\ell+1)}{3} \sum_{n'} \frac{\left|\langle n\ell|\frac{1}{r_2^3}|n'\ell\rangle\right|^2}{W_{5dn'\ell} - W_{6sn\ell}}$$
$$\left. \left. + (2\ell+3)(\ell^2-\ell) \sum_{n'} \frac{\left|\langle n\ell|\frac{1}{r_2^3}|n'\ell-2\rangle\right|^2}{W_{5dn'\ell-2} - W_{6sn\ell}} \right] \right\}. \quad (11)$$

TABLE VI. Quantum defects of $6sn\ell$ states.

n	$6sng$	$6snh$	$6sni$
28	0.026 062(8)		
29	0.026 074(9)	0.009 219(9)	0.003 912(14)
30	0.026 087(10)	0.009 224(10)	0.003 914(10)
31	0.026 097(11)	0.009 223(11)	0.003 933(12)
32	0.026 107(12)	0.009 237(12)	0.003 936(12)
33	0.026 117(13)	0.009 196(13)	0.003 997(19)

TABLE VII. Quantum defect parameters of the $6sn\ell$ series.

Series	δ_0	δ_1
$6sng$	0.026 257 4(25)	−0.153 3(22)
$6snh$	0.009 305(33)	−0.073(31)
$6sni$	0.004 062(36)	−0.128(34)

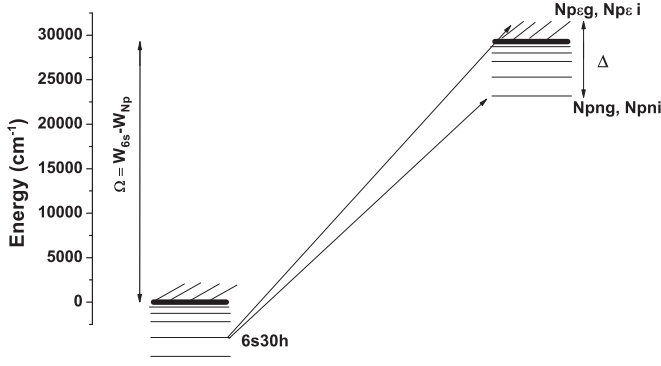FIG. 9. Schematic Yb energy levels. For each level of the Yb$^+$ core NL (bold line), there are Rydberg series ($NLn\ell$) converging to the ionic level from below and continua ($NL\epsilon\ell$) converging to the ionic level from above. The $6s30h$ state is dipole coupled to the $Npng$ and $Npni$ states and the $Np\epsilon g$ and $Np\epsilon i$ continua by the Rydberg electron and the ion core interaction. The total dipole shift of the $6s30h$ state due to the Rydberg states associated with the ionic Np levels is calculated by using the second-order perturbation of the dipole coupling and summing over all n and integrating over the continua ϵ. The summation and integration span the energy range Δ. In the limit where the span of energy is much less than the ionic energy level, $\Delta \ll \Omega$, the adiabatic equation, Eq. (4), is valid.

In the adiabatic limit, $\Delta \ll \Omega$, the energy denominators in the summations of Eqs. (10) and (11) can be removed from the summations and cancel the energy differences in the prefactors. Thus, the summations contain only squared radial matrix elements, and it is straightforward to show that in this limit $k_d = k_q = 1$. In Table VIII and Table IX we present the calculated values for k_d and k_q. These values were calculated numerically using hydrogen wave functions and a Numerov algorithm. We checked our numerical calculation using [25]

$$\sum_{n'} \langle n'\ell'|r^s|n\ell\rangle^2 = \langle n\ell|r^{2s}|n\ell\rangle. \quad (12)$$

The errors in calculation were determined to be less than 0.1%. The k_d values have no n dependence to four significant digits and the k_q values have no n dependence to three significant digits.

For simplicity of notation we introduce the following adaptations of $P_{n\ell}$ and $Q_{n\ell}$:

$$P'_{n\ell} = R_{\mathrm{Yb}}k_d\langle r^{-4}\rangle_{n\ell} \quad (13)$$

and

$$Q'_{n\ell} = \frac{k_q\langle r^{-6}\rangle_{n\ell}}{k_d\langle r^{-4}\rangle_{n\ell}}. \quad (14)$$

With these definitions we can rewrite Eq. (9) as

$$-\frac{W_{\mathrm{pol},n\ell}}{P'_{n\ell}} = \alpha_d + \alpha_q Q'_{n\ell}. \quad (15)$$

TABLE VIII. k_d calculated values.

$\ell = 4$	$\ell = 5$	$\ell = 6$
0.9375	0.9576	0.9733

TABLE IX. k_q calculated values.

$\ell = 4$	$\ell = 5$	$\ell = 6$
0.947	0.894	0.921

The polarization energies $W_{\mathrm{pol},n\ell}$ are determined from Table V. Combining the analytically known values of $\langle r^{-4}\rangle$ and $\langle r^{-6}\rangle$ with the values of k_d and k_q from Tables VIII and IX we can calculate $P'_{n\ell}$ and $Q'_{n\ell}$. Using $W_{\mathrm{pol},n\ell}$, $P'_{n\ell}$, and $Q'_{n\ell}$ we plot a graph of $-\frac{W_{\mathrm{pol},n\ell}}{P'_{n\ell}}$ vs $Q'_{n\ell}$ as shown in Fig. 10. From the intercept and slope of the line through the data points in Fig. 10, we determine the dipole and quadrupole polarizabilities of Yb$^+$ $6s$ to be $\alpha_d = 60.31(10)a_0^3$ and $\alpha_q = 659(28)a_0^5$, respectively. We ignore the ng series due to the possibilities of core penetration and interseries interactions with low-lying states converging to higher limits, and we exclude the $n = 33\ell$ states as these data exhibit an inconsistent n scaling.

As mentioned earlier, assuming that α_d and α_q arise solely from coupling to the $6pn'\ell$ and $5dn'\ell$ states introduces small errors. For α_d the largest error is due to the contribution of the Yb^{++} polarizability, which is calculated to be $6.4a_0^3$. It is not subject to the nonadiabatic correction; i.e., $k_d = 1$ for this part of α_d, not 0.97. Accordingly, the value of α_d obtained from Fig. 10 is too low by $0.2a_0^3$, and the correct value is

$$\alpha_d = 60.51(10)a_0^3. \quad (16)$$

For Yb$^+$ there has been no calculation of α_q. However, we have estimated that the contributions to α_q from couplings to the $Ndn'\ell$ states of $N \geqslant 6$ represent 20% of α_q. This fraction is similar to those calculated for Ca$^+$ and Sr$^+$ [17,22]. Since these contributions are not subject to as large a nonadiabatic correction, they should have $k_q \approx 1$, not $k_q = 0.9$. Accordingly, we raise the value of α_q obtained from Fig. 10 by 2%,
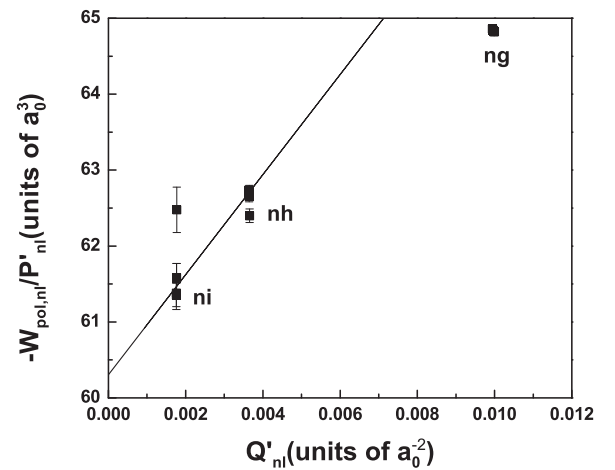

FIG. 10. Plot of $-W_{\mathrm{pol},n\ell}/P'_{n\ell}$ vs $Q'_{n\ell}$. From the nonadiabatic treatment of the ion core, Eq. (15), the plot can be fitted linearly. The intercept of the graph is α_d, and the slope of the graph is α_q. We determine α_d and α_q to be $60.31(10)a_0^3$ and $659(28)a_0^5$, respectively. Note that the ng data are omitted in the fit due to the core penetration of the ng states, and we omit $n = 33$ states as they are already inconsistent.

to yield

$$\alpha_q = 672(28)a_0^5. \tag{17}$$

There are theoretical predictions for the value of α_d. Reference [28] predicts the value of α_d to be $62.04a_0^3$. Reference [29] extracts the Yb$^+$ electric dipole matrix elements E1 $\langle 6s_{1/2}|r|6p_{3/2,1/2}\rangle$ from the lifetime measurements of the $6p_{1/2,3/2}$ levels in the Yb$^+$ ion of Refs. [30] and [31] to calculate α_d, yielding $\alpha_d = 59.3(8)a_0^3$. Our direct measurement value of α_d falls between the two predictions. To our knowledge, there is no measurement or theoretical prediction of α_q for the Yb$^+$ $6s$ state.

VI. CONCLUSION

We have measured the microwave and RF transitions of ytterbium from the $6s(n+3)d$ states to the $6sng$, $6snh$, and $6sni$ states for $28 \leqslant n \leqslant 33$. From the observed measurements, we use the precise values of the nd quantum defects to determine the precise energy levels and the quantum defects of the measured $n\ell$ states. We apply the nonadiabatic core polarization model to these energy levels to determine the Yb$^+$ $6s$ ionic dipole (α_d) and quadrupole (α_q) polarizabilities. We determine the values of α_d and α_q to be $\alpha_d = 60.51(10)a_0^3$ and $\alpha_q = 672(28)a_0^5$, respectively. Our α_d agrees well with the theoretical predictions.

[1] J. Stenger, C. Tamm, N. Haverkamp, S. Weyers, and H. R. Telle, Opt. Lett. **26**, 1589 (2001).

[2] R. M. Godun, P. B. R. Nisbet-Jones, J. M. Jones, S. A. King, L. A. M. Johnson, H. S. Margolis, K. Szymaniec, S. N. Lea, K. Bongs, and P. Gill, Phys. Rev. Lett. **113**, 210801 (2014).

[3] M. Roberts, P. Taylor, G. P. Barwood, P. Gill, H. A. Klein, and W. R. C. Rowley, Phys. Rev. Lett. **78**, 1876 (1997).

[4] K. Hosaka, S. A. Webster, P. J. Blythe, A. Stannard, D. Beaton, H. S. Margolis, S. N. Lea, and P. Gill, IEEE Trans. Instrum. Meas. **54**, 759 (2005).

[5] T. Schneider, E. Peik, and Chr. Tamm, Phys. Rev. Lett. **94**, 230801 (2005).

[6] S. A. Webster, P. Taylor, M. Roberts, G. P. Barwood, and P. Gill, Phys. Rev. A **65**, 052501 (2002).

[7] P. J. Blythe, S. A. Webster, K. Hosaka, and P. Gill, J. Phys. B: At. Mol. Opt. Phys. **36**, 981 (2003).

[8] P. J. Blythe, S. A. Webster, H. S. Margolis, S. N. Lea, G. Huang, S.-K. Choi, W. R. C. Rowley, P. Gill, and R. S. Windeler, Phys. Rev. A **67**, 020501(R) (2003).

[9] P. Gill, G. P. Barwood, H. A. Klein, G. Huang, S. A. Webster, P. J. Blythe, K. Hosaka, S. N. Lea, and H. S. Margolis, Meas. Sci. Technol. **14**, 1174 (2003).

[10] K. Hosaka, S. A. Webster, A. Stannard, B. R. Walton, H. S. Margolis, and P. Gill, Phys. Rev. A **79**, 033403 (2009).

[11] S. A. King, R. M. Godun, S. A. Webster, H. S. Margolis, L. A. M. Johnson, K. Szymaniec, P. E. G. Baird, and P. Gill, New J. Phys. **14**, 013045 (2012).

[12] Chr. Tamm, S. Weyers, B. Lipphardt, and E. Peik, Phys. Rev. A **80**, 043403 (2009).

[13] Chr. Tamm, N. Huntemann, B. Lipphardt, V. Gerginov, N. Nemitz, M. Kazda, S. Weyers, and E. Peik, Phys. Rev. A **89**, 023820 (2014).

[14] V. A. Dzuba, V. V. Flambaum, M. S. Safronova, S. G. Porsev, T. Pruttivarasin, M. A. Hohensee, and H. Häffner, Nat. Phys. **12**, 465 (2016).

[15] B. K. Sahoo and B. P. Das, Phys. Rev. A **84**, 010502(R) (2011).

[16] E. G. Kim, J. Nunkaew, and T. F. Gallagher, Phys. Rev. A **89**, 062503 (2014).

[17] J. Nunkaew and T. F. Gallagher, Phys. Rev. A **91**, 042503 (2015).

[18] J. E. Mayer and M. G. Mayer, Phys. Rev. **43**, 605 (1933).

[19] H. Lehec, A. Zuliani, W. Maineult, E. Luc-Koenig, P. Pillet, P. Cheinet, F. Niyaz, and T. F. Gallagher, Phys. Rev. A **98**, 062506 (2018).

[20] T. F. Gallagher, L. M. Humphrey, W. E. Cooke, R. M. Hill, and S. A. Edelstein, Phys. Rev. A **16**, 1098 (1977).

[21] E. S. Shuman, J. Nunkaew, and T. F. Gallagher, Phys. Rev. A **75**, 044501 (2007).

[22] J. Nunkaew, E. S. Shuman, and T. F. Gallagher, Phys. Rev. A **79**, 054501 (2009).

[23] E. S. Shuman and T. F. Gallagher, Phys. Rev. A **74**, 022502 (2006).

[24] B. Edlen, *Handbuch der Physik* (Springer, Berlin, 1964).

[25] J. H. Van Vleck and N. G. Whitelaw, Phys. Rev. **44**, 551 (1933).

[26] S. R. Lundeen, in *Advances in Atomic, Molecular, and Optical Physics*, edited by P. R. Berman and C. C. Lin (Elsevier Academic, Amsterdam, 2005), Vol. 52, pp. 161–208.

[27] T. F. Gallagher, R. Kachru, and N. H. Tran, Phys. Rev. A **26**, 2611 (1982).

[28] U. I. Safronova and M. S. Safronova, Phys. Rev. A **79**, 022512 (2009).

[29] A. Roy, S. De Bindiya Arora, and B. K. Sahoo, J. Phys. B: At. Mol. Opt. Phys. **50**, 205201 (2017).

[30] S. Olmschenk, D. Hayes, D. N. Matsukevich, P. Maunz, D. L. Moehring, K. C. Younge, and C. Monroe, Phys. Rev. A **80**, 022502 (2009).

[31] E. H. Pinnington, G. Rieger, and J. A. Kernahan, Phys. Rev. A **56**, 2421 (1997).